Activated carbon synthesized from Jack wood biochar for high performing biomass derived composite double layer supercapacitors

Carbon Trends 15 (2024) 100359

Contents lists available at ScienceDirect

Carbon Trends

journal homepage: www.elsevier.com/locate/cartre

Activated carbon synthesized from Jack wood biochar for high performing biomass derived composite double layer supercapacitors

T.M.W.J. Bandara [a,*], A.M.B.S. Alahakoon [a], B.-E. Mellander [b], I. Albinsson [c]

[a] Department of Physics and Postgraduate Institute of Science, University of Peradeniya, Peradeniya, Sri Lanka
[b] Department of Physics, Chalmers University of Technology, Gothenburg, Sweden
[c] Department of Physics, University of Gothenburg, Gothenburg, Sweden

ARTICLE INFO

Keywords:
Supercapacitors
Activated carbon
Electrochemical double-layer capacitors
Cyclic voltammetry
Jack wood biochar
TiO_2 binder

ABSTRACT

In this study, the electrochemical properties of bioderived activated carbon-based electrodes for supercapacitors formed using a sintered ceramic binder were investigated. Activated carbon derived from Jack wood tree (*Artocarpus heterophyllus*) with variable amounts of TiO_2 nanoparticles as a binder, were used as electrodes in order to get good, activated carbon films on FTO substrates. No other binders were used in this study since most conventional binders devastate the electrical conductivity in the films. Furthermore, TiO_2 has higher temperature tolerance compared to polymeric binders thus the electrode prepared can be used in wider applications. A series of electrochemical double-layer capacitors were fabricated and characterized by cyclic voltammetry and galvanostatic charge-discharge measurements. The supercapacitors prepared showed double-layer capacitive behavior. The electrodes that contain 90 % activated carbon and 10 % TiO_2 show optimum performance along with an impressive specific capacitance of 147 F g^{-1} at 2 mV s^{-1} scan rate. This supercapacitor exhibits a power density of 68.5 W kg^{-1} while the energy density is 8.02 Wh kg^{-1}. When the power density is as high as 1186.51 W kg^{-1} the energy density drops to 5.71 Wh kg^{-1}. According to cyclic voltammetry measurements taken for 1000 cycles, the supercapacitor shows excellent cycle stability without any traces of capacitance drop.

1. Introduction

Supercapacitors attract attention due to their longer cycle life, higher charge/discharge rates, use of less hazardous materials and safety compared to secondary batteries. Activated carbon is used as electrode material in supercapacitors due to its facile synthesis, high surface area and porosity, low cost, high conductivity, high physical and chemical stability, and high mechanical strength. etc [1]. Most of the commercial grade activated carbons are derivatives of fossil fuel products, and the synthesis needs well-controlled reaction conditions, and they are thus expensive and non-biodegradable. On the other hand, activated carbon produced from biomass is widely used in applications like water purification etc, however, their use in electrochemical energy storage devices is still lacking [2,3].

Depending on the ways in which energy is stored, supercapacitors are mainly divided into double-layer capacitors (EDLCs) and pseudo-capacitors, which can be distinguished by their charge storage mechanism. In general, EDLCs show a non-faradic reaction with the accumulation of charges/ions at the electrode-electrolyte interface, while pseudo-capacitors demonstrate reversible and faradaic redox reactions at the interface [4]. However, in practical EDLCs capacitance is lower compared to their theoretical limits and energy density is lower compared to typical secondary batteries. Carbonaceous materials [5,6], transition metal oxides [7-9], and conductive polymers [10,11] are widely used to prepare supercapacitor electrodes due to their favorable properties [12,13].

Fig. 1 represents the graphical representation of the mechanisms involved in supercapacitors [1]. An electrochemical supercapacitor consists of two electrodes, which are kept apart by a separator between them (Fig. 1) and these two electrodes are identical for a symmetric supercapacitor (Fig. 1 (a)) but solely different for an asymmetric supercapacitor as presented in Fig. 1 (b) and 1 (c) [14]. In pseudocapacitors, fast, reversible faradaic redox reactions occur at the interface of the electrolyte and nanostructured metal oxide or conductive polymer electrodes (Fig. 1 (b)). Hybrid capacitor charge storage arises from fast reversible faradaic redox reactions and non-Faradaic electrostatic interactions at the electrode/electrolyte interface (Fig. 1 (c)). Hybrid supercapacitors are produced by combining oxide electrodes or

* Corresponding author.
E-mail address: wijendra@sci.pdn.ac.lk (T.M.W.J. Bandara).

https://doi.org/10.1016/j.cartre.2024.100359
Received 6 February 2024; Received in revised form 15 April 2024; Accepted 29 April 2024
Available online 1 May 2024

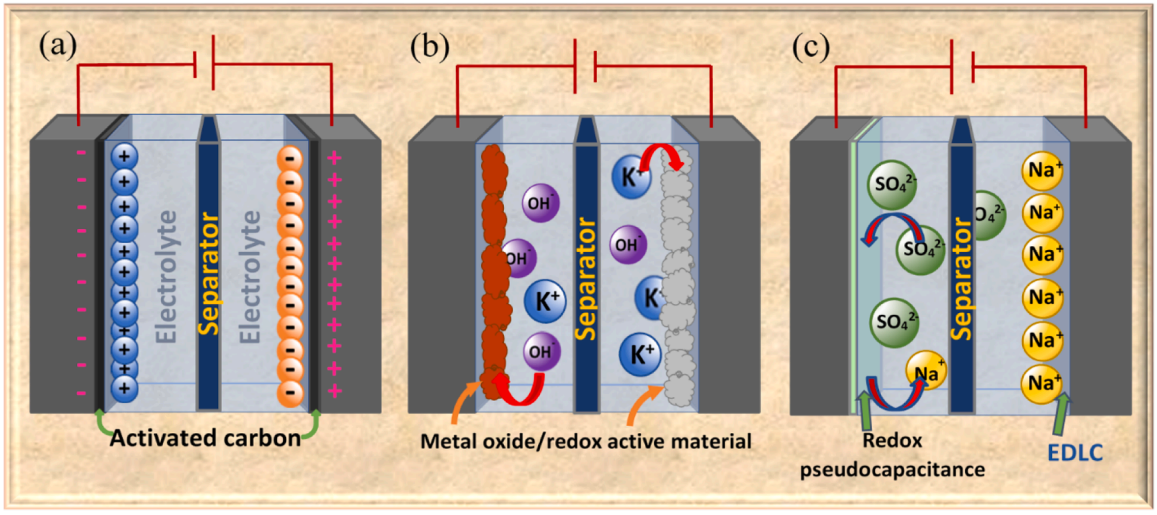

Fig. 1. Schematic diagram to illustrate the charge storage mechanism of (a) EDLC, (b) Pseudocapacitor and (c) Hybrid Capacitor.

Fig. 2. Photographic images of (a) NaOH solution of impregnated activated carbon, (b) heated carbon solution, (c) neutralized activated carbon solution by washing with deionized water and stainless-steel container, (d) sample is in horizontal tube furnace and (e) prepared activated carbon.

conductive polymers with carbon-based materials. In general, the separator is ion-permeable, and also electrically insulating, which is soaked with electrolytes to allow ionic charge transfer between two electrodes. Polymer or paper separators are often used with organic electrolytes while ceramic or glass-fiber separators are preferred for aqueous electrolytes [14].

The capacitance response of a supercapacitor with a high charging-discharging rate (or high CV scan rate) is a key factor for achieving practical application in the electrochemical supercapacitor since the high-power demand for modern electronic power tools and electric vehicles, etc. In addition, to accomplish the realization of a high-performing supercapacitor, finding a suitable electrolyte is another important factor. Liquid electrolytes are popular compared to other electrolytes in the field of supercapacitors since the high mobility of ions increases the performance. Most of the experiments have been conducted using either an acidic electrolyte such as H_2SO_4 or a strong basic electrolyte such as KOH. Generally, the electrical double-layer formation and the capacitance strongly depend on the type and concentration of the electrolyte used and the surface area emerging from the porous structure of the carbon in the electrode. Besides, the H_2SO_4-based electrolyte, which demonstrates better ionic diffusion into the pores of the carbon, since the presence of H^+ ions as the mobile species, results in an enhanced EDLC performance [4]. In addition, aqueous EDLCs perform a high specific capacitance compared to non-aqueous EDLCs because the molecular size of organic electrolytes is larger than aqueous electrolytes, which affects the mobility of the ions [15].

The working potential is a crucial factor that affects the performance of aqueous EDLCs. The decomposition of H_2O takes place at 1.23 V, which greatly obstructs the performance of the storage device [15]. Because of this reason, in general, operating voltages were kept below 1 V for the CV and GCD measurements. However, the operating voltage window for organic electrolytes-based supercapacitors can be as high as 0 V to 2.5–2.7 V. The maximum potential limit depends upon the nature of electrode materials and the stability of electrolytes used for the storage device [16].

Various electrode materials can be tried out to improve the electrochemical responses of electrodes since the transfer kinetics between electrode and electrolyte depends mainly on the chemical and physical properties of the electrode and electrode material [17]. As such, changing the electrode material is a proper approach to improve the performance of supercapacitors. Further various biomass-derived carbon materials are used in energy storage applications due to their environmental friendliness, high and natural abundance lower cost, and porous structures [17]. In this study, activated carbon derived by carbonizing Artocarpus heterophyllus (commonly known as Jack wood), is used to prepare a new biomass-derived porous carbon electrode for EDLCs. To the best of our knowledge, the biomass of Jack wood trees hasn't been used for the preparation of supercapacitor-grade activated carbon or other applications. Furthermore, the synthesis of biomass-derived carbon is conducted using simple low-cost methods, which involve pyrolysis at 800 °C for 1 h. The present work introduces a relatively facile method to prepare supercapacitors using biomass-derived activated carbon reporting remarkably higher energy and power densities for an activated carbon-based EDLC.

2. Experimental

2.1. Preparation of activated carbon

Thin wooden stripes were derived from Jack tree (*Artocarpus heterophyllus*) wood and were carbonized completely under ambient atmospheric conditions. Then the carbonized samples were crushed and ground to make a carbon powder. The resulting powder product was then added to NaOH (~2.5 mol dm^{-3}) solution. The weight ratio of carbonized samples to NaOH was 1:1 in the mixed system. Next, the solution was stirred and kept at room temperature for 48 hours. A stainless-steel container was used to put the precursor in, which was then placed in a horizontal tube furnace and the activation was performed at 800 °C for 1 h. After cooling down, the yield was thoroughly washed with 0.1 M HCl, and subsequently washed with deionized water many times to remove residual NaOH until the pH of the wash water reached 7 and finally dried in vacuum at 120 °C for 24 h. Photographic images of (a) NaOH solution of impregnated activated carbon, (b) heated carbon solution, (c) neutralized activated carbon solution by washing with deionized water and stainless-steel container, (d) sample in horizontal tube furnace and (e) prepared activated carbon are given in Fig. 2 for the clear illustration of yields and steps.

Table 1
Weight percentages of Activated Carbon and TiO_2 in the precursor paste.

Electrodes	Activated carbon (g)	TiO_2 (g)	Activated carbon (wt %)	$TiO_{2\ \%}$ (wt %)
A	0.09	0.01	90	10
B	0.08	0.02	80	20
C	0.07	0.03	70	30
D	0.06	0.04	60	40
E	0.05	0.05	50	50

2.2. Preparation of supercapacitor electrodes

A series of composite supercapacitor electrodes were prepared using a mixture of activated carbon and TiO_2 powder. Table 1 shows mass fractions of TiO_2 nanoparticles of the particle size 21 nm (Sigma-Aldrich AEROXIDE® TiO_2 P 25) and prepared activated carbon used for the supercapacitor electrode preparation. The compounds were mixed in 1 ml of 1 M HNO_3 solvent for 24 hours under vigorous stirring. The precursor yield was then coated on the conducting side of the precleaned FTO (Fluorine-doped Tin Oxide) substrate covering an area of 1 cm^2 using the drop cast method. Then, the activated carbon-coated FTOs were immediately annealed at 100 °C for 30 min. Activated carbon electrodes could not be prepared using slurries having more than 90 % activated carbon content due to poor film formation and weak adhesivity to the FTO substrate. The mass of the active materials was obtained by measuring the weight difference of the electrodes before and after the coating process. Then, the prepared electrodes were used to characterize and assemble EDLCs.

2.3. Activated carbon-based EDLC

A series of symmetric EDLCs were fabricated by sandwiching a piece of Whatman® 1 filter paper between the two supercapacitor electrodes. Then the filter paper was wetted with a 1 M H_2SO_4 electrolyte solution.

2.4. Characterization

The electrochemical impedance spectroscopy measurement was performed by an electrochemical analyzer (Autolab, PGSTAT128N) over a frequency range from 0.01 Hz to 100 kHz at an activated carbon amplitude of 10 mV. The impedance data were utilized to determine the polarization effects of the electrolyte. In addition, the structural characterization of activated carbon/TiO_2 composite electrodes was done with thin film X-Ray diffraction (XRD) with CuKα X-Ray radiation (λ = 15.406 nm) using the Rigaku Ultima IV X-ray diffractometer. The morphology of the samples was observed using scanning electron microscopy (SEM, Zeiss evo-LS15) images. A Thermo ScientificTM ESCALAB Xi+ X-ray Photoelectron Spectrometer (XPS) is used to obtain XPS spectra of the samples.

2.5. Electrochemical measurements

The electrochemical measurements were performed using a

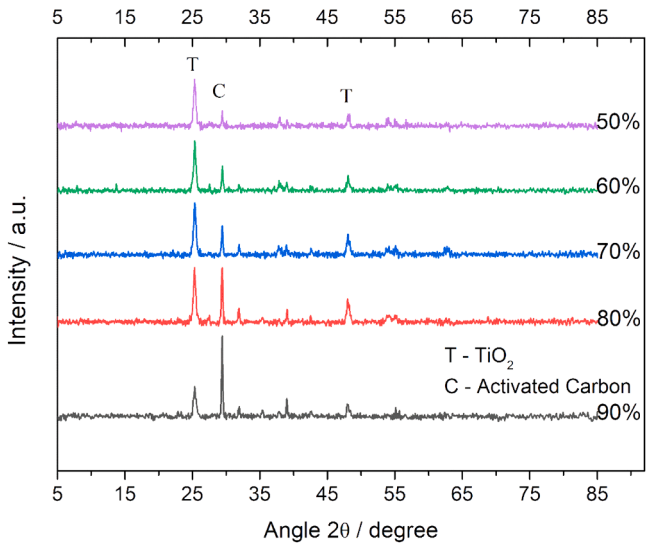

Fig. 3. XRD spectra of supercapacitor electrode series prepared with different mass fractions of activated carbon (50, 60, 70, 80 and 90 %) and TiO_2 (50, 40, 30, 20 and 10 %) on FTO substrate.

computer-controlled Metrohm Autolab Electrochemical Analyzer (128 N series) in a two-electrode system. The electrodes of supercapacitors are connected to the potentiostat, once the cells have been assembled and the experimental parameters are selected through the NOVA software. The cyclic voltammetry (CV) measurements were carried out over a potential range from 0 V to 0.8 V at the scan rates from 2 to 100 mV s^{-1}. The equation,

$$C_{sp} = \frac{2\int IdV}{m\Delta V \frac{dV}{dt}} \quad (1)$$

was used to calculate the supercapacitor capacitance (C_{sp}), where m is the mass of the activated carbon layer on the single electrode, I is current, ΔV is the potential range used and $\frac{dV}{dt}$ is the potential scan rate used in the CV experiments [18].

Further, galvanostatic charge-discharge (GCD) curves were obtained within the potential range of 0–1 V at different current densities. All the electrochemical measurements were carried out at room temperature. 1 M H_2SO_4 solution served as the electrolyte for all supercapacitors studied in this work. The specific capacitance Cs (F g^{-1}) of activated carbon in the symmetric supercapacitor prepared were calculated by substituting the parameters obtained from GCD measurements in the equation [19],

$$C_{sp} = \frac{4I}{m\ dV/dt} \quad (2)$$

where I (A) is the constant discharge current, m (g) is the total mass of active material in two electrodes, and dV/dt (V s^{-1}) is the gradient of the discharge curve which is obtained by linear fitting of the discharge curve.

The energy density E (W h kg^{-1}) and power density P (W kg^{-1}) of the supercapacitors were calculated following Eqs. 2 and 3, respectively [20,21].

$$E = \frac{1}{2} C\ \Delta V^2 \quad (3)$$

$$P = \frac{E}{\Delta t} \quad (4)$$

where ΔV (V) is the potential window and Δt (s) is the discharge time.

Table 2
Relative peak intensities of XRD spectra with respect to the peak at 2θ = 29.4° of sample A.

Angle (2θ°)	Sample A (%)	Sample B (%)	Sample C (%)	Sample D (%)	Sample E (%)
29.41[a]	100.0[a]	65.2	33.4	27.6	18.7
25.35	35.7	64.7	59.1	58.5	58.4
48.06	15.7	26.7	24.0	16.9	14.7

Table 3
The average crystallite size (D), and d Spacing calculated utilizing XRD data.

Angle (2θ°)	Crystal plane	d Spacing (Å)	D (nm)
29.41	C (013)	3.0	40. 8
25.35	T (101)	3.5	17.5
48.06	T (200)	1.9	19.0

3. Results and discussion

3.1. Characterization of electrodes

3.1.1. XRD analysis

XRD analyses were performed to investigate the effects of the composition on the structure of the activated carbon and TiO_2 films. The XRD patterns of the activated carbon and TiO_2 composite electrodes are shown in Fig. 3 for the electrodes prepared by varying mass fractions of activated carbon and TiO_2. In XRD patterns, peaks are intense at the 2θ value of 25.3° and 29.4° which are characteristic of TiO_2 and non-amorphous carbon/graphite, respectively. The intense peak at 25.3° that grows with the increasing amount of TiO_2 indicates the anatase (101) crystal planes of TiO_2 tetragonal lattice structure (ICSD; PDF 01–070–7348) [22,23]. The sharp peak (C-peak) at 29.4° corresponds to the (013) crystal plane of carbon orthorhombic lattice structure (ICSD; PDF 01–080–4909) in which the intensity abates with the increasing amount of TiO_2. The less intensive peak at 48.0° is due to the reflection of TiO_2 (200) crystal planes. Furthermore, the relative intensities of the peaks associated with TiO_2 (101), and (200), and carbon (013) are given in Table 2 (ICSD; PDF 01–070–7348, PDF 01–080–4909). The peak intensities were calculated with respect to the peak at 29.4° of sample A and given in Table 2. As expected, the intensity of the carbon peak diminishes with the reducing amount of carbon, while TiO_2 peaks are intensifying with the increase in the amount of TiO_2. However, a slight broadening of the TiO_2 peaks can be observed compared to the carbon peaks. This minor broadening could be due to the smaller crystallite size of TiO_2 relative to the carbon in electrode materials.

The average crystallite size (D) and d spacing were calculated utilizing the Debye–Scherrer equation and Bragg's law [22,24]. The calculated values for respect diffraction peaks are given in Table 3. According to the results, the crystallite size of the TiO_2 varies slightly and the calculated particle size is 17.5 and 19.0 nm for anatase (101) and (200), while the average crystallite size of carbon is about 40.8 nm.

3.1.2. SEM images

Fig. 4 shows SEM images taken of activated carbon/TiO_2 films prepared on FTO substrates. No significant structural or morphological differences were observed in Fig. 4 (a)–(e), that is for samples with 10 to 50 % TiO_2 at magnification 5000. A granular activated carbon distribution with various sizes and shapes is observed in Fig. 4 (a)–(e). The size of the activated carbon particles is of the order of several micrometers, and between these larger activated carbon particles the presence of some smaller activated carbon particles is observed. For better clarity, SEM images taken at 25,000 magnifications are also shown in Fig. 4 (f)–(j). The presence of smaller activated carbon particles and pores are visible in samples A and B (Fig. 4 (a), (b), (f), and (g)) and these images correspond to the electrodes with lower TiO_2 contents. When the TiO_2

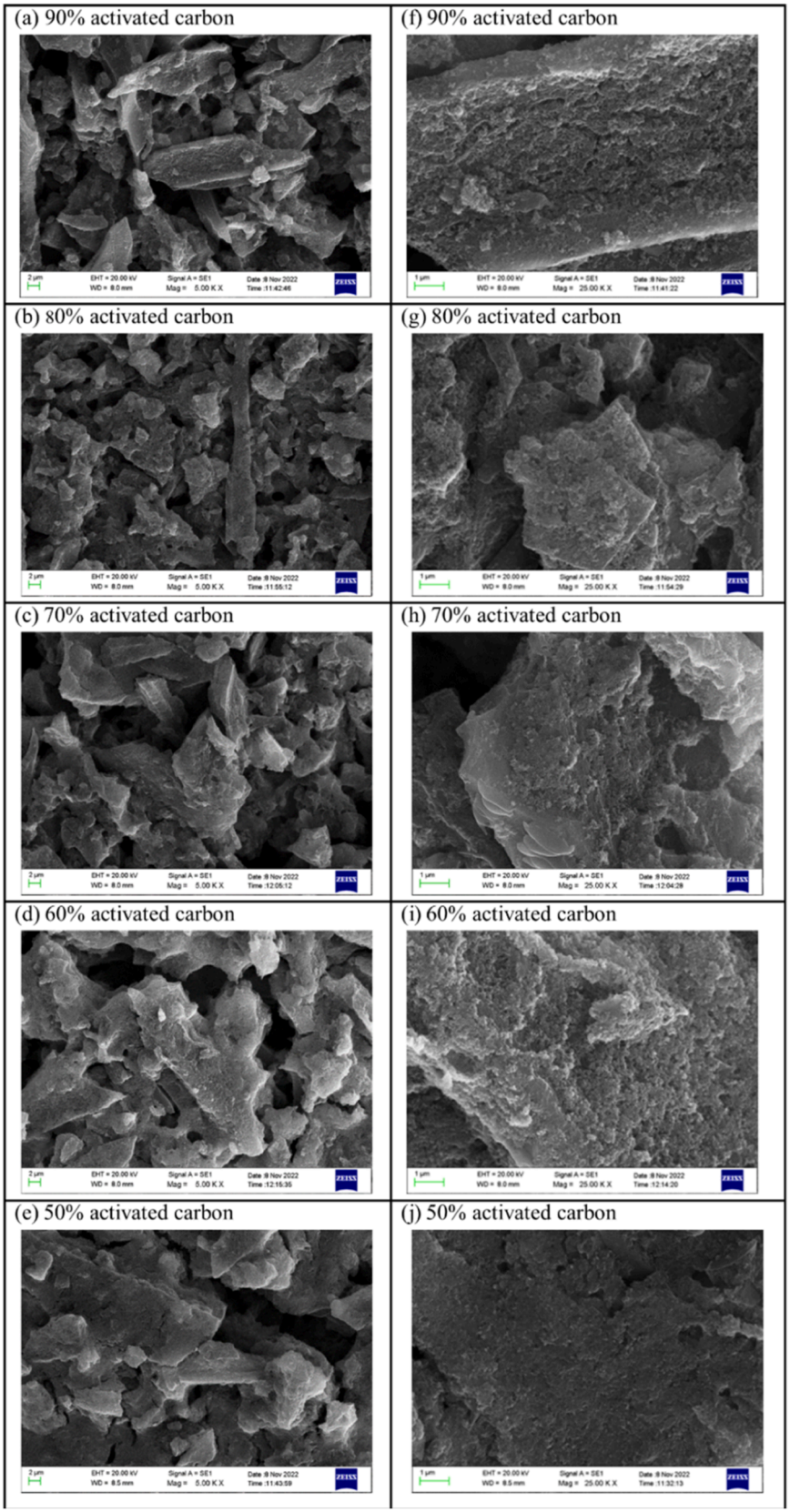

Fig. 4. SEM images of activated carbon/TiO_2 films (a) A (10 % TiO_2), (b) B (20 % TiO_2), (c) C (30 % TiO_2), (d) D (40 % TiO_2), and (e) E (50 % TiO_2) prepared by drop-cast method on FTO substrates captured at a magnification of 5000. SEM taken at 25,000 magnification are shown in (f), (g), (h) (i), and (j), for samples (A), (B), (C), (D) and (E), respectively.

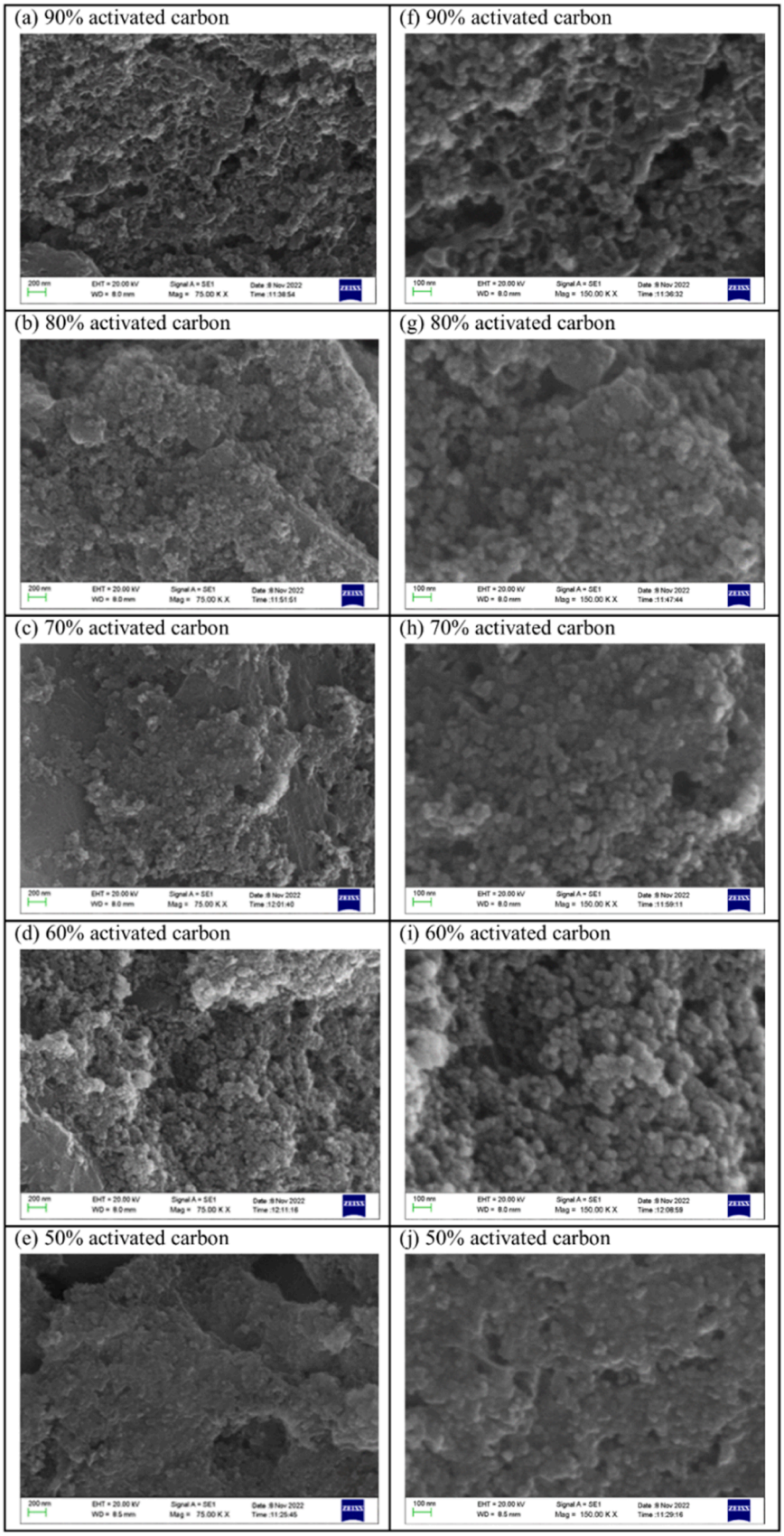

Fig. 5. The SEM images of activated carbon/ TiO_2 films (a) A (10 % TiO_2), (b) B (20 % TiO_2), (c) C (30 % TiO_2), (d) D (40 % TiO_2), and (e) E (50 % TiO_2), prepared on FTO and taken at a magnification of 75,000. Respective SEM taken at magnification 150,000 are shown in (f), (g), (h) (i), and (j).

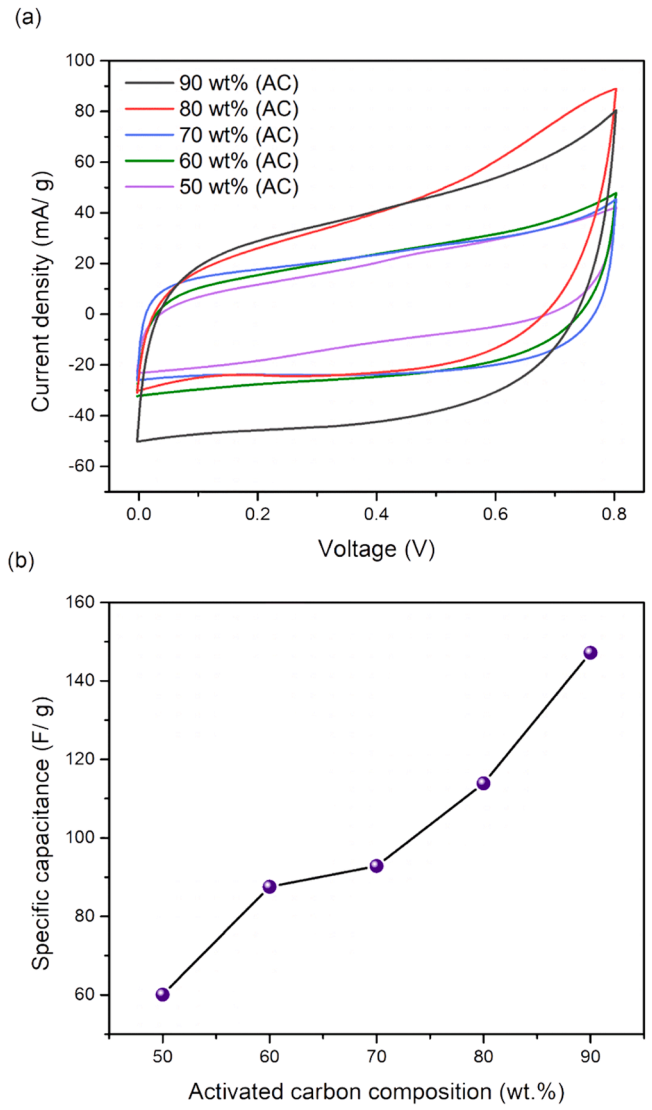

Fig. 6. (a) CV cycles of supercapacitors assembled using electrodes that contain different mass fractions of activated carbon (50, 60, 70, 80, and 90 %) and TiO_2 (50, 40, 30, 20, and 10 %), measured at 2 mV s^{-1}. (b) Specific capacitance versus activated carbon composition of the supercapacitor electrode series.

content is increased, samples D and E (Fig. 4 (d), (e), (i) and (j)), these small particles and small pores in the films are covered by layers of TiO_2 that provide structural interconnection to activated carbon particles. Therefore, neither small pores nor very small particles are seen on activated carbon surfaces in samples D and E. However, larger pores and particles are still visible in the sample. However, a macroporous morphology can be seen among carbon particles in all the samples. As per the images, it looks like the granular type of activated carbon particles were cemented by the smaller TiO_2 particles. Due to the high porosity, the material has a large effective surface area, making it well-suited for use in EDLC preparation.

In order to get a detailed understanding of the films and to get an idea about the role of TiO_2 as the binder SEM images of activated carbon/TiO_2 films prepared on FTO substrates and taken at magnification 75,000 are shown in Fig. 5 (a)–(e). Images taken at magnification 150,000 are shown in Fig. 5 (f)–(j). A granular type activated carbon distribution is visible in Fig. 4 and these granular elements were well bonded by the TiO_2 slurry as seen in Fig. 5. The distribution of TiO_2 provides a geometrical structure to hold activated carbon particles. The TiO_2 structures formed by interconnected TiO_2 nanoparticles of the size

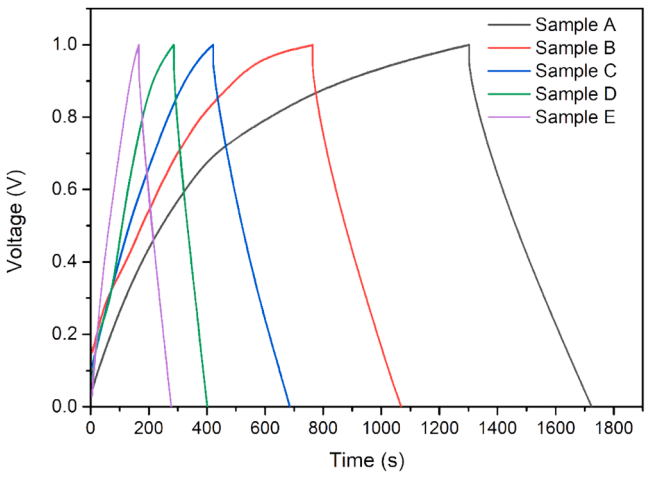

Fig. 7. GCD curves of supercapacitor series assembled using electrodes that contain different mass fractions of activated carbon (50, 60, 70, 80, and 90 %) and TiO_2 (50, 40, 30, 20, and 10 %) respectively at a current density of 0.5 mA cm^{-2}.

21 nm (as of the manufacturer specifications) are firm after the calcination of the samples. We did not manage to make films when the TiO_2 content was below 10 % because of insufficient binder content. The TiO_2 content in sample A is barely enough to form a layer as seen in Fig. 5 (a)–(f). In samples B and C also, there are some uncovered activated carbon particle surfaces by the TiO_2. The smaller activated carbon particles and pores of about 50–100 nm are visible on activated carbon in sample A, (Fig. 5 (a) and (f)) which correspond to the lowest TiO_2 content out of the tested samples. In samples D and E which have higher TiO_2 content, the smaller activated carbon particles and smaller pores of activated carbon are covered by the spread TiO_2 as seen in Fig. 5 (d), (e), (i), and (j). Finally, it can be inferred that the granular type of activated carbon particles were bonded by the smaller interconnected network of TiO_2 particles. TiO_2 layers also show nanoporous structure. Due to the high porosity in and among activated carbon particles, the films can offer a large effective surface area, making them well-suited for use in EDLC preparation.

3.2. *Electrochemical performance*

3.2.1. *Optimization of electrode composition*

3.2.1.1. CV curves. Fig. 6 (a) depicts the comparison of the CV curves of all supercapacitors prepared by varying the activated carbon content in the electrode and taken at a scan rate of 2 mV s^{-1}. All the CV curves display a rectangular shape and rapid current responses upon voltage reversal, manifesting excellent EDLC behavior. According to the CV plots, electrodes containing 90 wt.% activated carbon- shows the largest enclosed area among the electrodes studied under the same scan rate. This indicates that this electrode (90 wt.% activated carbon) acquires the highest charge storage capacity which can be a result of relatively high carbon content in the electrode [25]. The specific capacitances of supercapacitors were calculated using the parameters obtained from the CV measurements and Eq. 1 see Fig. 6 (b) [26]. As shown in the Figure the specific capacitance of supercapacitors increases with the increasing amount of activated carbon and decreasing amount of TiO_2. In this study, TiO_2 nanoparticles were added to the electrode-preparing slurry, in order to get good, activated carbon films on FTO substrates. No binders were used in this work since most binders devastate the electrical conductivity in the films. In addition, TiO_2 has a higher temperature tolerance compared to polymeric binders. When the activated carbon content is increased above 90 %, we did not manage to get stable films on FTO substrates and thus supercapacitors could not be prepared.

Table 4
The IR drop and specific capacitance obtained from the GCD curves at the current density of 0.5 mA cm^{-2} of the supercapacitor series.

Electrode	IR drop (V)	Specific capacitance (F g^{-1})
A	0.050	57.79
B	0.052	51.09
C	0.054	50.70
D	0.056	37.30
E	0.059	37.03

Supercapacitors assembled using the electrode that contains 90 wt.% activated carbon and 10 wt.% TiO_2 showed the highest specific capacity of 147.2 F g^{-1} at 2 mV s^{-1} scan rate.

3.2.1.2. GCD curves. Fig. 7 shows the GCD curves of the supercapacitor series studied in this work by varying activated carbon and TiO_2 contents in the electrodes and measured under a current density of 0.5 mA cm^{-2}. The IR drop and specific capacitance obtained from the GCD curves are given in Table 4. All the supercapacitors exhibited specific capacitance above 37 F g^{-1}. The supercapacitor made with sample A that contains 90 % activated carbon showed the highest specific capacitance of 57.8 F g^{-1} under 0.5 mA cm^{-2} current density out of the series investigated.

3.2.2. Characterization of the optimized supercapacitor

3.2.2.1. CV at different scan rates. Cyclic voltammetry (CV) taken at 2, 5, 10, 20, 50 and 100 mv s^{-1} scan rates of the supercapacitor assembled using an electrode that contains activated carbon (90 wt.%) and TiO_2 (10 wt.%) are shown in Fig. 8 (a). It can be seen that all curves are smooth and there are no traces of any redox peaks. Therefore, CV plots confirm that charge storage takes place electrostatically without any redox reactions occurring in the potential window of 0.0 V to 0.8 V [27-29]. This implies an electrochemical double-layer (EDLC) behavior of the supercapacitor and also reveals that the electrolyte is stabilized, and no significant decomposition within the working voltage range. Moreover, the CV plots, shown in Fig. 8 (a), reveal that the curve retains its rectangular shape even at the higher scan rate of about 20 mV s^{-1}, which clarifies the unbounded motion of electrolyte species in the pores at the slow double-layer formation situation [30]. However, the rectangular shape of the curve is distorted when the scan rate is increased above 50 mV s^{-1}. The behavior can be attributed to higher resistance for the motion of electrolytic ions in porous carbon layers. To achieve higher charge storage ions must be efficiently distributed forming the double-layer formation all over the surface to give rectangular EDLC behavior at high scan rates [30,31].

The areas enclosed by each CV curve in Fig. 8 (a) are tabulated in Table 5. The specific capacitances calculated using CV curves are plotted in Fig. 8 (b) as a function of the scan rate. The specific capacitance of the optimized supercapacitor is 147.2 F g^{-1} at 2 mV s^{-1}. However specific capacitance decreases with increasing scan rate as a result of relaxation effects of charge transport, in particular, since the deep penetrating ions take a longer time to permeate into the porous carbon. Thus, faster scan rates cause a decrease in the size of the diffusion layer by hindering the specific capacitance [32]. Conversely, higher currents are observed in the CV curves obtained at higher scan rates as a result of the rapid increase of applied potential difference and thus resulted in faster velocity of ions. The drop of capacitance at higher rates can be due to the accumulation of charges on the electrode surface without penetrating into deep pores due to the faster cycling process. Therefore, a decrease in specific capacitance is observed with increasing scan rate as a result of charge transport relaxation effects.

3.2.2.2. GCD at different current densities. The galvanostatic charge-discharge (GCD) performance of the supercapacitor made using the electrodes composed of 90 wt.% activated carbon and TiO_2 10 wt.% were measured at the current densities of 0.5, 1, 2, 3, 4, and 5 mA cm^{-2}. The GCD curves are presented in Fig. 9 (a). It can be observed that all supercapacitors exhibit more or less triangular-shaped charge/discharge curves which are highly symmetrical and linear at increased current densities, indicating a typical characteristic of an ideal electrical double-layer capacitor & further showing its exceptional capacitive reversibility, which also agrees with the analysis results of the CV curves [30]. The initial section (drop) of the discharge curve displays an IR drop produced by internal resistance and the rest of the curve will be nearly linear for non-faradic electrode materials [33]. Specific capacitances calculated from the GCD curves at different current densities are shown in Fig. 9 (b). The specific capacitance decreases with the increase in the

Table 5
Area enclosed by the CV curve of the supercapacitors that contains activated carbon (90 wt.%) and TiO_2 (10 wt.%).

Scan rate (mV s^{-1})	Area enclosed by CV curve (10^{-4} × mW)
2	6.47
5	13.67
10	22.17
20	31.92
50	36.96
100	29.93

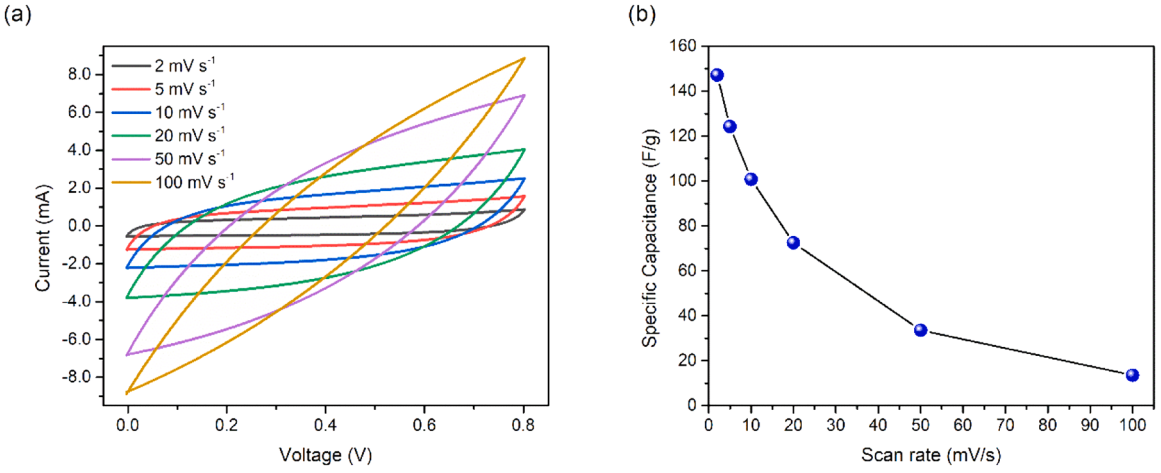

Fig. 8. (a) Cyclic voltammograms of the supercapacitor that contains activated carbon (90 wt.%) and TiO_2 (10 wt.%), at different scan rates. (b) specific capacitance as a function of scan rate.

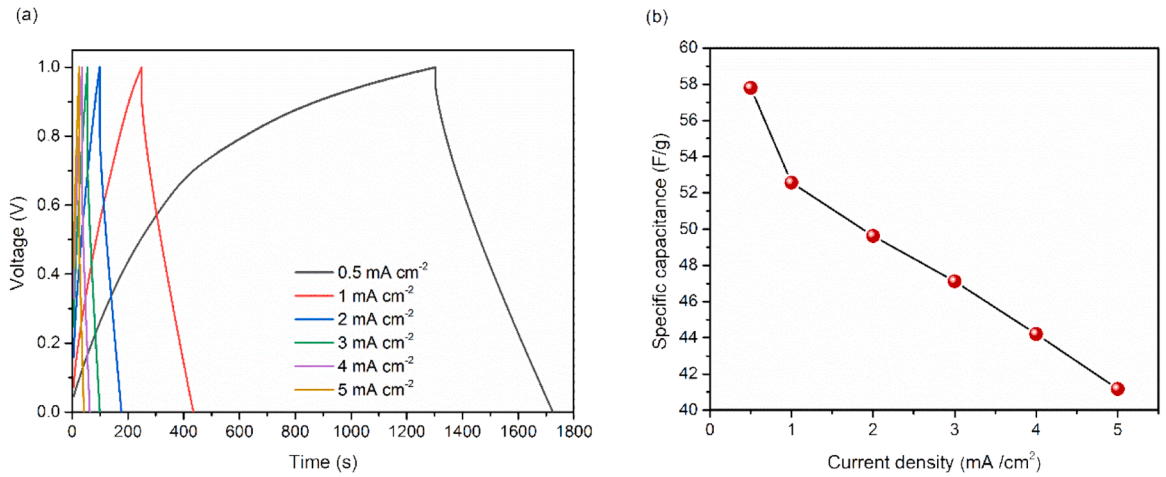

Fig. 9. (a) GCD curves of the supercapacitor that contain activated carbon (90 wt.%) and TiO_2 (10 wt.%), at different current densities. (b) specific capacitance obtained from GCD curves against current densities.

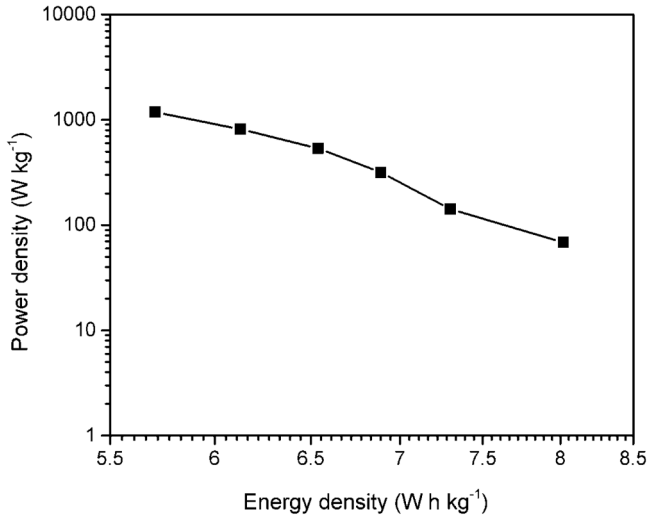

Fig. 10. Power density vs energy density of the supercapacitor that contains activated carbon (90 wt.%) and TiO_2 (10 wt.%).

current density, which mainly causes an incremental voltage drop in the discharge curves. The maximum specific capacitance of 57.8 F g^{-1} is shown when the current density is as low as 0.5 mA cm^{-2} which decreases to 51.2 F g^{-1} when the current density increases by one order of magnitude. When lower currents are used for the charge/discharge process, it takes longer time for the charging and discharging allowing slow carries and deep penetrating carries to participate in the formation of EDLC and thus increase the capacity.

3.2.2.3. Energy density and power density. Energy density and power density are two important factors to determine the performance of supercapacitor devices. Energy density and power density were calculated using GCD measurements and Eqs. (3) and (4) and, respectively. Calculated energy and power densities are given in Table 7 as a function of current density. The increase in the discharge current causes a shorter discharge time, hence increase in the power density is observed. The energy density versus power density curves of the supercapacitors prepared in this work using the electrode composed of 90 wt.% activated carbon and 10 wt.% TiO_2 are presented in Fig. 10. The prepared supercapacitor showed a power density of 68.5 W kg^{-1} along with an energy density of 8.02 W h kg^{-1} at the current density of 0.5 mA cm^{-2}. It can exhibit a power density as high as 1186.5 W kg^{-1} at 5.71 W h kg^{-1} energy density at the current density of 5 mA cm^{-2}.

Table 6
Energy densities and power densities and capacitances of some EDLCs reported along with the values obtained in this study.

Electrode Material	Electrolyte	Power density (W kg^{-1})	Energy density (W h kg^{-1})	Capacitance (F g^{-1})	Ref.
AC	0.5 M Na_2SO_4	-	10	135 at 0.2 A g^{-1}	[34]
AC	4 M $NaNO_3$-EG 2	~500	14–16	22.3 at 2 mV s^{-1}	[35]
Microporous carbon	0.5 M Na_2SO_4	~40	~7	~60 at 0.2 A g^{-1}	[36]
AC	1 M $NaNO_3$	-	-	116 at 2 mV s^{-1}	[37]
MMPGC	2 M H_2SO_4	20	4	105 at 4 mV s^{-1}	[38]
AC fibers	1 M H_2SO_4	-	-	280 at 0.5 A g^{-1}	[39]
Walnut peel	-	5679.62	12.44	557.9 at 1 A g^{-1}	[40]
AC	1 M H_2SO_4	-	-	24 at 0.25 A g^{-1}	[41]
Porous carbon nanofibers	-	125	12	344 at 1 A g^{-1}	[42]
BC/PEDOT/ CNT fiber	PVA H_3PO_4	120.1	4	175.1 at 5 mV s^{-1}	[43]
AC (this study)	1 M H_2SO_4	68.6	8.0	147 at 2 mV s^{-1}	
AC (this study)	1 M H_2SO_4	1186.5	5.7	147 at 2 mV s^{-1}	

AC-based EDLCs showed specific capacitance in the range of 50–150 F g^{-1} and 100–200 F g^{-1} with organic electrolytes and aqueous electrolytes respectively and they have exhibited capacitances of 225 and 160 Fg^{-1}. In order to compare the performance of the EDLC prepared in

Table 7
Calculated results for energy and power densities for different current densities.

Current density (mA cm^{-2})	Energy density (W h kg^{-1})	Power density (W kg^{-1})
0.5	8.02	68.47
1.0	7.30	142.06
2.0	6.89	316.60
3.0	6.54	536.13
4.0	6.13	814.99
5.0	5.71	1186.51

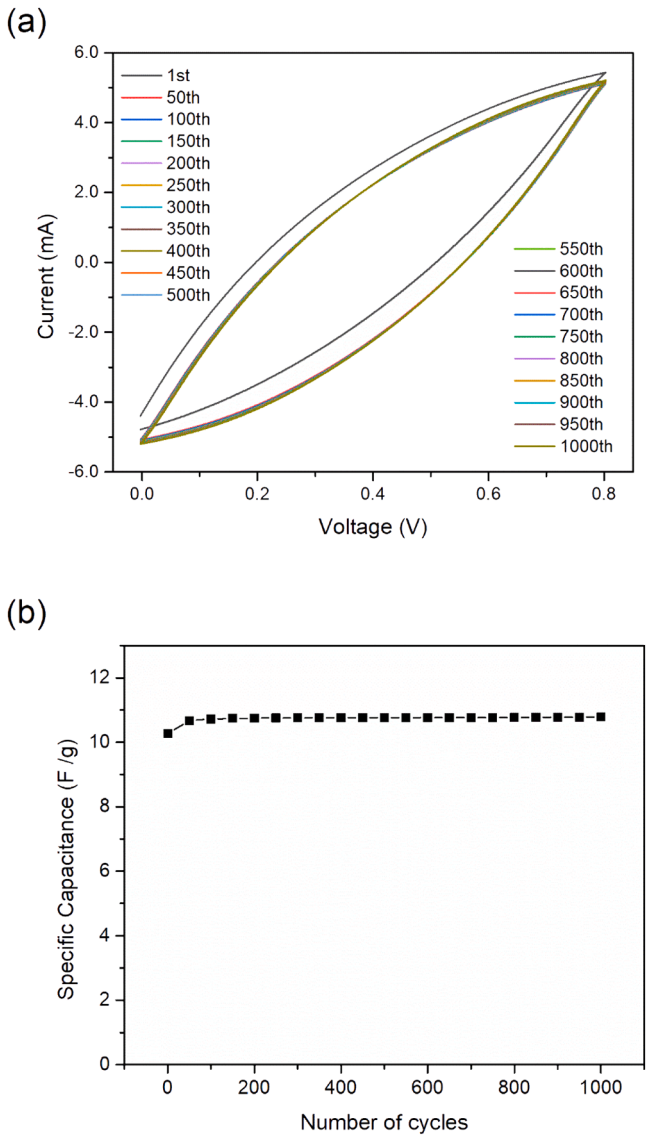

Fig. 11. The cycling performance of the optimized supercapacitor at scan rate 100 mV s^{-1} for 1000 cycles (data are shown in 50 steps). (a) CV curves measured at 100 mV s^{-1} for 1000 cycles (b) specific capacitance against the number of cycles.

this study some power density, energy density and specific capacitance values of EDLCs reported are given in Table 6 along with the values obtained in this study (Table 7).

3.2.2.3. *Cycling stability of the supercapacitor*

3.2.2.3.1. Cyclic voltammetry. The supercapacitor prepared using electrode composition of activated carbon (90 wt.%) and TiO_2 (10 wt.%) showed the highest specific capacitance and the cells were used to investigate the cycling stability. CVs at every 50 steps up to 1000 cycles are shown in Fig. 11 (a) and the capacitance against cycle number is given in Fig. 11 (b) Further, the data presented in Fig. 11 (Capacitance vs. the number of cycles). The cells exhibited ~105 % capacitance retention after 1000 cycles implying excellent cycling stability the excellent cycle life. Rapid capacitance improvement observed with 1st 50 cycles can be due to the heating effects. However, after 50 cycles the EDLC exhibited almost constant capacitance up to 1000 cycles. This measurement was taken at a scan rate of 100 mVs^{-1} considering the time it takes to complete 1000 cycles.

The Nyquist plots of the supercapacitor prepared using the electrode

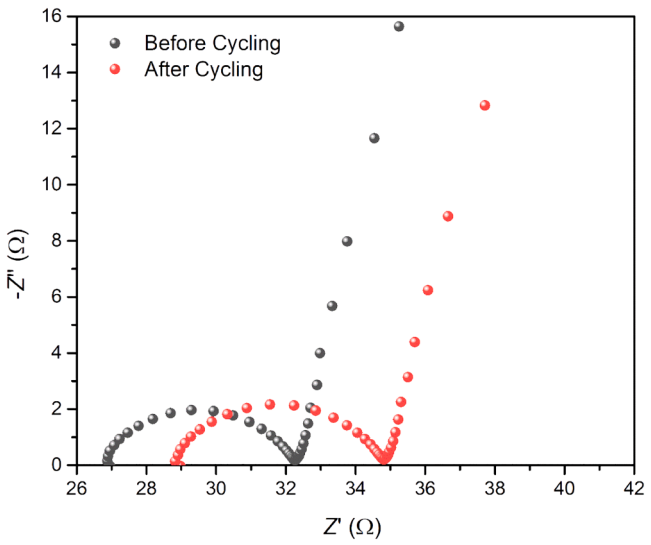

Fig. 12. Nyquist plots of the supercapacitor prepared by 90 wt% (activated carbon) sample before and after the 1000 CV cycles were performed.

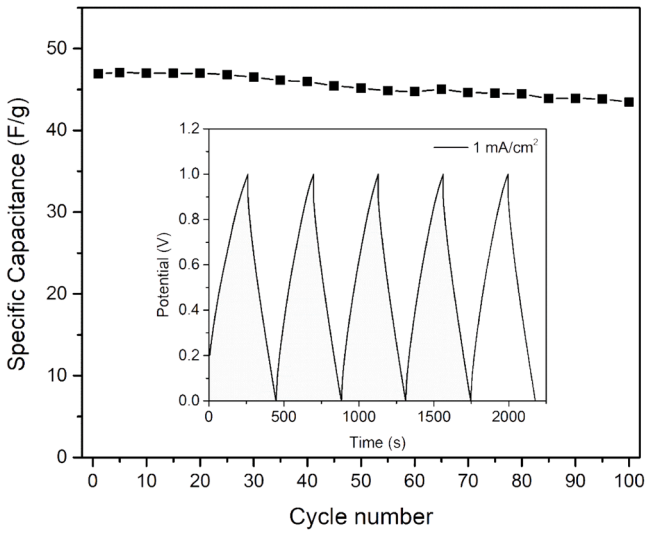

Fig. 13. Cycling performance of the supercapacitor prepared using electrode composition of activated carbon (90 wt.%) and TiO_2 (10 wt.%) at the current density of 3 mA/cm^2 up to 100 cycles. Inset: Typical GCD cycling at a constant current of 1 mA/cm^2 in the first five cycles.

having 90 wt% (activated carbon) before and after the 1000 CV cycles are shown in Fig. 12. The high-frequency resistance R_s, which corresponds to electronic transport has slightly increased from 26.88 to 28.83 Ω during the cycle stability test. The diameter of the semicircle (small semicircle) corresponds to the charge transport resistance (R_{ct}) in the electrolyte has increased from 5.38 to 6.01 Ω. Since these resistances have increased with the cycling process the observed capacitance increase can be attributed to the heating effect due to prolonged cycling.

3.2.2.3.2. Galvanostatic charge-discharge. Further, continuously repeating GCDs were collected to check the charge-discharge performance of the optimized supercapacitors. Capacitance against the charge /discharge cycle number is shown in Fig. 13 for 100 repetitions. supercapacitor exhibits excellent charge /discharge cyclic stability giving specific capacitance retention of 92.58 % under a current density of 3 mA cm^{-2}. The observed slight decrease in the specific capacitance can be due to changes in the structure and composition of active materials in the electrodes as well as the electrolyte [21]. Further, it can be due to the

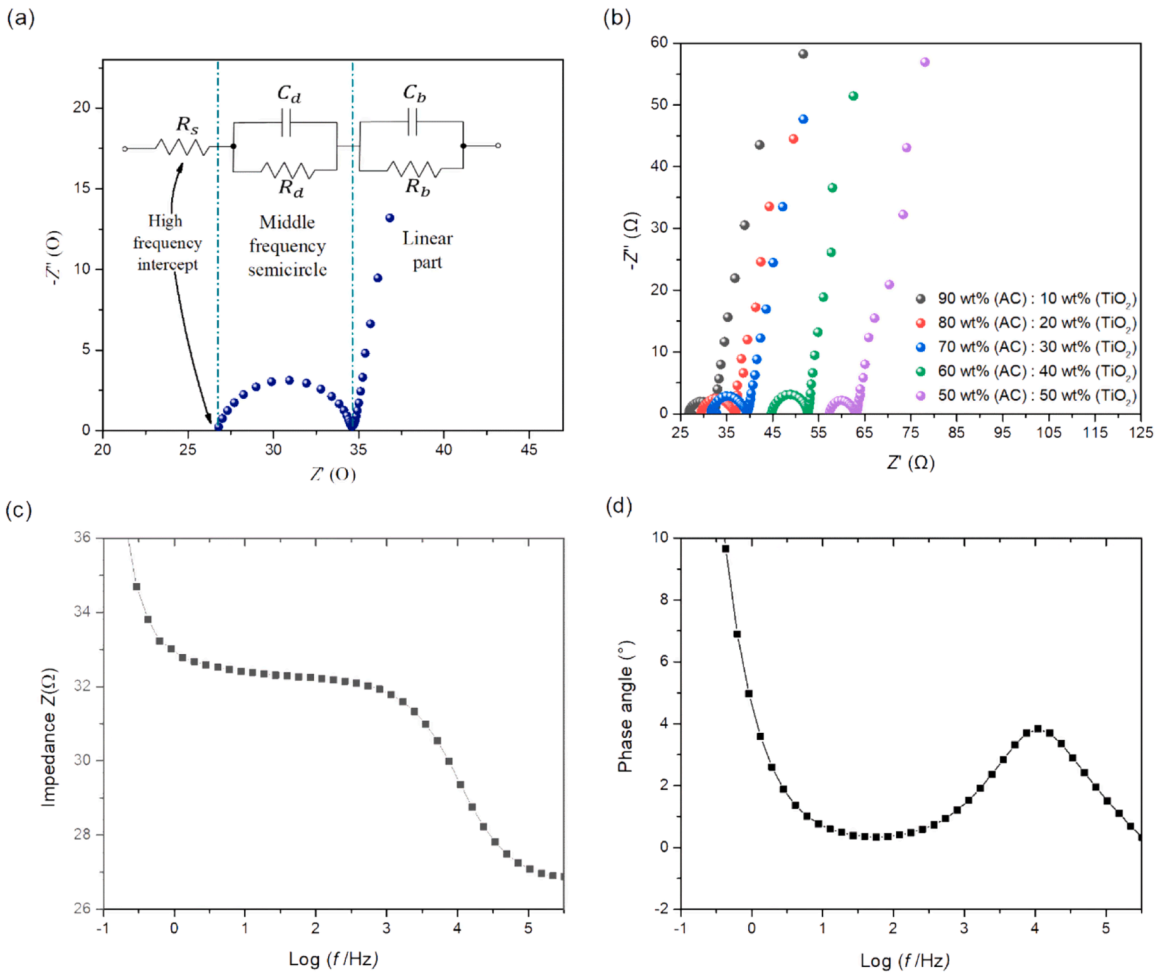

Fig. 14. (a) Bode plot of 90 wt% (activated carbon) sample. (b) Nyquist plots of the five different supercapacitors prepared by varying the activated carbon and TiO_2 concentrations in the electrodes. (c) Equivalent circuit model of supercapacitors.

resistive energy loss due to heating effects.

3.2.2.3.3. Electrochemical impedance spectroscopy (EIS). Electrochemical impedance data of the EDLC is shown in Fig. 14. Fig 14 (a) illustrates the equivalent circuit model used for the data analysis. Nyquist plots of the five different supercapacitors prepared by varying the activated carbon and TiO_2 concentrations in the electrodes are shown in Fig 14 (b) while Fig 14 (c)and (d) shows the Bode plot of the 90 wt% (activated carbon) containing sample. Electrochemical impedance spectroscopy (EIS) is a well-established technique to investigate the electrical properties of electrodes and to determine the parameters involving the performance of an electrode such as conductivity, charge-transfer, and diffusion properties [44]. Nyquist plots of the supercapacitors at frequencies from 0.01 Hz to 100 kHz are shown in Fig. 14 (b). Nyquist plots show a depressed semicircle in the high-frequency region and a straight line in the low-frequency region. The internal resistance (R_s) can be determined by the interception of the high-frequency region at the real axis, which is a combinational resistance of intrinsic resistances of the substrate (current collector), activated carbon/TiO_2 electrode, and leads. and contact resistance at the interface between the current collector and active materials [44,45]. According to the Nyquist plot, the R_s values for 90 wt.%, 80 wt.%, 70 wt.%, 60 wt.%, and 50 wt.% activated carbon are 26.9 Ω, 29.4 Ω, 32.0 Ω, 44.7 Ω and 57.3 Ω, respectively. These relatively high resistances shown for higher TiO_2 content can be attributed to the increased resistance of the electrode film with added poorly conductive TiO_2. In the high-frequency region, the diameter of the semicircle (small semicircle) corresponds to the charge transport resistance (R_{ct}) in the electrolyte. R_{ct} values for 90 wt.%, 80 wt.%, 70 wt.%, 60 wt.%, and 50 wt.% activated carbon are 5.31 Ω, 7.35 Ω, 7.34 Ω, 7.81 Ω, 5.72 Ω, respectively. Low R_{ct} values depict low internal resistance and fast charge transfer kinetics [21]. The straight line which is more or less vertical in the low-frequency range is due to the effect of the EDLC behavior of the electrodes [46]. The linear nature of the low-frequency region (infinite radius of the semicircle) indicates an extremely high interfacial charge transfer resistance between the double layers. Therefore, the leakage current between double layers is negligible in these supercapacitors.

3.2.2.3.4. XPS analysis. XPS analysis was conducted to identify the oxidation states of the elements of the SC electrode. For this purpose, an electrode prepared with 90 wt% AC and 10 wt% TiO_2 sample was utilized. XPS survey was performed across a broader range to identify the elements present in the sample as shown in Fig. 15 (a). Three distinct peaks corresponding to oxygen (O 1 s), carbon (C 1 s), and titanium (Ti 2p) were observed in the spectrum. High-resolution scans were then performed to assess the surface functional and relative content of the SC electrode. The high-resolution XPS spectra correspond to O 1 s, depicted in Fig. 15 (b) which exhibit a peak corresponding to C=O having a binding energy of 530.75 eV [47]. The peak at 529.45 eV corresponds to the O-Ti bond in TiO_2 [52].

According to Fig. 15 (c), a strong peak occurred at 281.8 eV, and a weak peak appeared at 287.0 eV. The peak at 281.8 eV can be attributed to carbon in the C-Ti bonds in the sample [48]. The Ti-C bond arises from the substitution of oxygen atoms by carbon, indicating carbon substituting for oxygen atoms in the lattice of titanium dioxide, forming the O-Ti-C bond [49]. Peaks at 283.5 eV and 284.6 eV can be assigned to

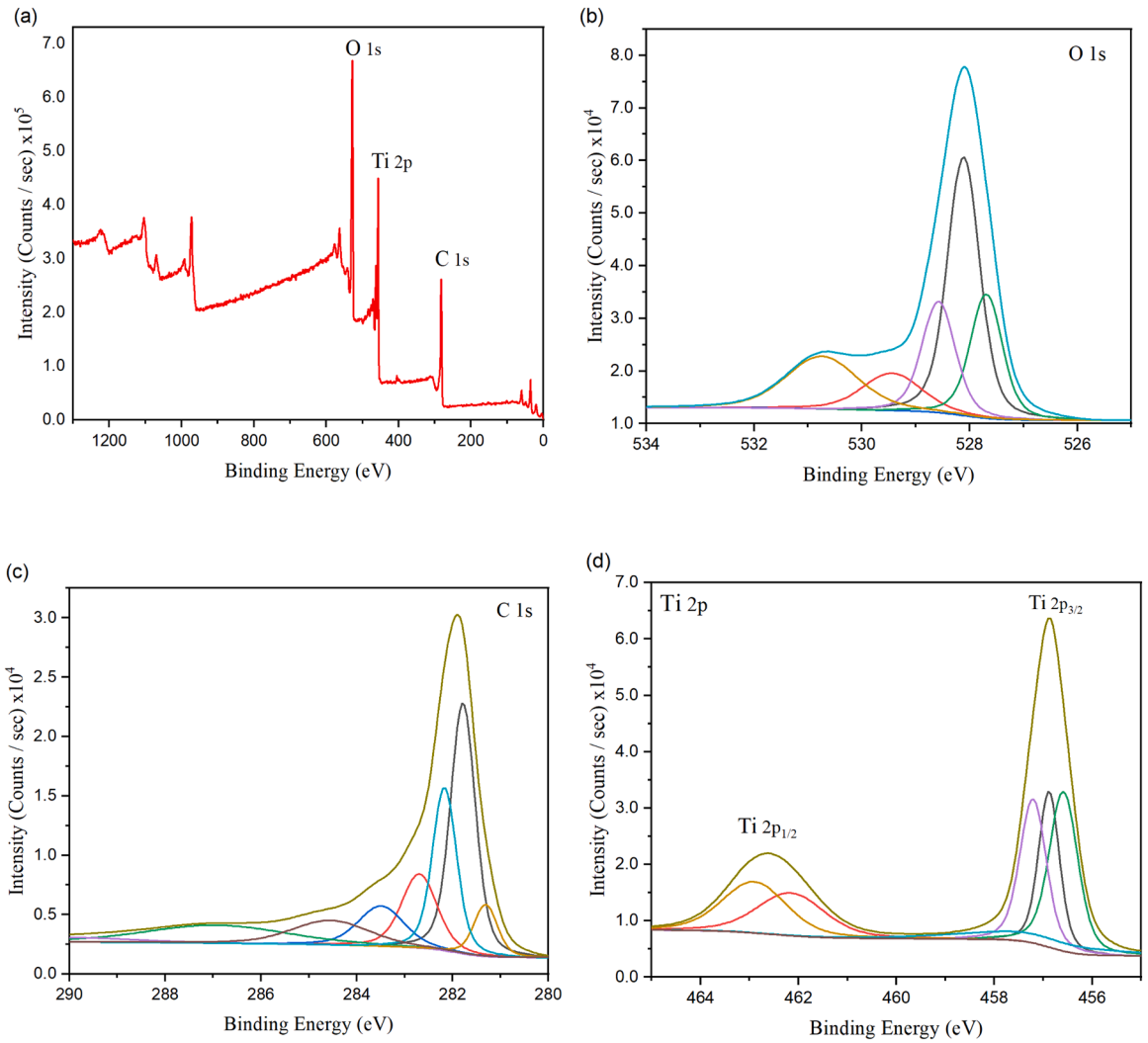

Fig. 15. (a) XPS survey spectra (b) High resolution O 1 s spectra, (c) High resolution spectra of C 1 s peaks, and (d) High resolution spectra of Ti 2p peaks of the electrode that contains 90 % AC and 10 % TiO_2.

adventitious carbon species originating from the organic precursor, corresponding to graphitic carbon with mainly C-C bonds [50,51].

The high resolution XPS spectrum of Ti 2p is shown in Fig. 15 (d), which shows two peaks at 456.9 and 462.6 eV, corresponding to the Ti $2p_{3/2}$ and Ti $2p_{1/2}$ states of stoichiometric TiO_2. According to the deconvolution results, the peaks located at about 457.20 eV (Ti $2p_{3/2}$) and 462.95 eV (Ti $2p_{1/2}$) are associated with Ti^{3+} species, corresponding to C–Ti^{3+}-(O/OH), and those of Ti^{2+} species are located at around 456.6 eV (Ti $2p_{3/2}$) and 462.2 eV (Ti $2p_{1/2}$), correspond to C–Ti^{2+}–(O/OH) [52]. The binding energy difference can be calculated using the following equation,

$$\Delta E_b = E_b\left(\mathrm{Ti}\,2p_{1/2}\right) - E_b\left(\mathrm{Ti}\,2p_{3/2}\right) \quad (5)$$

The value consistently around 5.7 eV, indicating the standard binding energy for the Ti element [53]. Fig. 15 (d) illustrates that the content of Ti^{3+} and Ti^{2+} is relatively high, implying the presence of amorphous Ti_2O_3 in the thin film.

In summary, these biomaterial-derived activated carbon-based electrodes were prepared successfully using TiO_2 as a film-forming substance. The supercapacitors showed high specific capacitance and for electrodes with 10 % TiO_2 and 90 % activated carbon, the optimum specific capacitance was obtained. In addition, it showed good capacitance retention. The study uncovers a way of preparing low-cost polymeric binder-free electrodes for supercapacitors.

4. Conclusion

Activated carbon was prepared from local jack-wood by carbonization and subsequent activation with NaOH. Activation is conducted to get high porosity and high effective surface area for carbon, which was then used to synthesize the electrochemical double-layer capacitors for the first-time using jack wood-derived activated carbon electrodes. Polymeric binders were not used in this work since most such binders hinder the electrical conductivity in the films due to their solubility in electrolytes. Instead, it was found that TiO_2 can be used as a binder. In addition, TiO_2 has higher temperature tolerance compared to polymeric binders and thus it is suitable for high-temperature devices. In addition, novel supercapacitor electrodes, such as flexible electrodes, have been prepared using polymer binders subjected to complex processes to obtain thin films on the electrodes, which can be quite costly. In comparison, the process followed in this study is simple and cost-effective. The X-ray diffraction (XRD) depicted polycrystalline anatase phases of TiO_2, peaks related to a crystalline phase of carbon. The size of the average TiO_2 crystallites was of the order of 18–19 nm and this value is about 40 nm for the carbon. A series of composite supercapacitor electrodes were prepared by changing the composition (activated carbon/TiO_2) and were tested by assembling activated carbon-based

supercapacitors. The results show double-layer capacitive behaviors of supercapacitors with a high specific capacitance of 147 F g^{-1} at 2 mV s^{-1} scan rate with an aqueous H_2SO_4 electrolyte. The supercapacitors prepared with 90 % activated carbon and 10 % TiO_2 show the EDLC performances. Charge discharge measurements of the supercapacitor exhibit good rate capability and excellent cyclic stability while having a specific capacitance retention of 92.6 % for 100 cycles. Furthermore, the supercapacitor displayed a power density of 68.5 W kg^{-1} while having an energy density of 8.02 Wh kg^{-1} at the current density of 0.5 mA cm^{-2}. This EDLC exhibits power density as high as 1186.5 W kg^{-1} at 5.71 W h kg^{-1} energy density at the current density of 5 mA cm^{-2}. According to CV measurements, the supercapacitor improved in this work shows excellent cycle stability. The cells exhibited ~5 % capacitance improvement after 1000 cycles and there are no traces of capacitance drop within the cycle window.

Ethical approval

Not applicable

CRediT authorship contribution statement

T.M.W.J. Bandara: Writing – review & editing, Supervision, Project administration, Methodology, Funding acquisition, Data curation, Conceptualization. **A.M.B.S. Alahakoon:** Writing – original draft, Validation, Investigation. **B.-E. Mellander:** Writing – review & editing, Visualization, Conceptualization. **I. Albinsson:** Writing – review & editing, Validation, Funding acquisition.

Declaration of competing interest

The authors declare that they have no known competing financial interests or personal relationships that could have appeared to influence the work reported in this paper.

Data availability

Data will be made available on request.

Acknowledgments

The Authors gratefully acknowledge the financial support from the Swedish Research Council, Sweden, grant number 2021-04889, as well as from the Peradeniya University Research Council (URC) Multidisciplinary Research grant no 346.

Supplementary materials

Supplementary material associated with this article can be found, in the online version, at doi:10.1016/j.cartre.2024.100359.

References

[1] B. Pal, S. Yang, S. Ramesh, V. Thangadurai, R. Jose, Electrolyte selection for supercapacitive devices: a critical review, Nanoscale Adv. 1 (10) (2019) 3807–3835.
[2] S. Mandal, J. Hu, S.Q. Shi, A comprehensive review of hybrid supercapacitor from transition metal and industrial crop based activated carbon for energy storage applications, Mater. Today Commun. 34 (2023) 105207.
[3] T. Subramaniam, S.G. Krishnan, M.N.M. Ansari, N.A. Hamid, M. Khalid, Recent progress on supercapacitive performance of agrowaste fibers: a review, Criti. Rev. Solid State Mater. Sci. 48 (2) (2023) 289–331.
[4] V. Subramanian, C. Luo, A.M. Stephan, K.S. Nahm, S. Thomas, B. Wei, Supercapacitors from activated carbon derived from banana fibers, J. Phys. Chem. C 111 (20) (2007) 7527–7531.
[5] E. Dhandapani, S. Thangarasu, S. Ramesh, K. Ramesh, R. Vasudevan, N. Duraisamy, Recent development and prospective of carbonaceous material, conducting polymer and their composite electrode materials for supercapacitor—a review, J. Energy Storage 52 (2022) 104937.
[6] L. Liu, X. An, Z. Tian, G. Yang, S. Nie, Z. Shang, H. Cao, Z. Cheng, S. Wang, H. Liu, Y. Ni, Biomass derived carbonaceous materials with tailored superstructures designed for advanced supercapacitor electrodes, Ind. Crops. Prod. 187 (2022) 115457.
[7] B. De, S. Banerjee, K.D. Verma, T. Pal, P.K. Manna, K.K. Kar, Transition metal oxides as electrode materials for supercapacitors. Handbook of Nanocomposite Supercapacitor Materials II: Performance, 2020, pp. 89–111.
[8] V. Quispe-Garrido, G.A. Cerron-Calle, A. Bazan-Aguilar, J.G. Ruiz-Montoya, E. O. López, A.M. Baena-Moncada, Advances in the design and application of transition metal oxide-based supercapacitors, Open. Chem. 19 (1) (2021) 709–725.
[9] S.A. Delbari, L.S. Ghadimi, R. Hadi, S. Farhoudian, M. Nedaei, A. Babapoor, A. S. Namini, Q. Van Le, M. Shokouhimehr, M.S. Asl, M. Mohammadi, Transition metal oxide-based electrode materials for flexible supercapacitors: a review, J. Alloys. Compd. 857 (2021) 158281.
[10] S. Wustoni, D. Ohayon, A. Hermawan, A. Nuruddin, S. Inal, Y.S. Indartono, B. Yuliarto, Material design and characterization of conducting polymer-based supercapacitors, Polym. Rev. 64 (1) (2024) 192–250.
[11] M.G. Sumdani, M.R. Islam, A.N.A. Yahaya, S.I. Safie, Recent advancements in synthesis, properties, and applications of conductive polymers for electrochemical energy storage devices: a review, Polym. Eng. Sci. 62 (2) (2022) 269–303.
[12] P. Dulyaseree, V. Yordsri, W. Wongwiriyapan, Effects of microwave and oxygen plasma treatments on capacitive characteristics of supercapacitor based on multiwalled carbon nanotubes, Jpn. J. Appl. Phys. 55 (2S) (2016) 02BD05.
[13] E. Frackowiak, S. Delpeux, K. Jurewicz, K. Szostak, D. Cazorla-Amoros, F. Beguin, Enhanced capacitance of carbon nanotubes through chemical activation, Chem. Phys. Lett. 361 (1-2) (2002) 35–41.
[14] X. Chen, R. Paul, L. Dai, Carbon-based supercapacitors for efficient energy storage, Natl. Sci. Rev. 4 (3) (2017) 453–489.
[15] Y. Wang, L. Zhang, H. Hou, W. Xu, G. Duan, S. He, K. Liu, S. Jiang, Recent progress in carbon-based materials for supercapacitor electrodes: a review, J. Mater. Sci. 56 (2021) 173–200.
[16] P. Haldar, Achieving wide potential window and high capacitance for supercapacitors using different metal oxides (viz.: ZrO_2, WO_3 and V_2O_5) and their PANI/graphene composites with Na_2SO_4 electrolyte, Electrochim. Acta 381 (2021) 138221.
[17] P. Forouzandeh, V. Kumaravel, S.C. Pillai, Electrode materials for supercapacitors: a review of recent advances, Catalysts. 10 (9) (2020) 969.
[18] A. Jain, S.R. Manippady, R. Tang, H. Nishihara, K. Sobczak, V. Matejka, M. Michalska, Vanadium oxide nanorods as an electrode material for solid state supercapacitor, Sci. Rep. 12 (1) (2022) 21024.
[19] F. Zhang, T. Zhang, X. Yang, L. Zhang, K. Leng, Y. Huang, Y. Chen, A high-performance supercapacitor-battery hybrid energy storage device based on graphene-enhanced electrode materials with ultrahigh energy density, Energy Environ. Sci. 6 (5) (2013) 1623–1632.
[20] Y. Ma, D. Chen, Z. Fang, Y. Zheng, W. Li, S. Xu, X. Lu, G. Shao, Q. Liu, W. Yang, High energy density and extremely stable supercapacitors based on carbon aerogels with 100% capacitance retention up to 65,000 cycles, Proceed. Natl. Acad. Sci. 118 (21) (2021) e2105610118.
[21] Y. Li, L. Li, F. Du, Amorphous S-doped NixCo3-xO4 for high-performance asymmetric supercapacitors, Electrochim. Acta 434 (2022) 141326.
[22] T.M.W.J. Bandara, L.A. DeSilva, J.L. Ratnasekera, K.H. Hettiarachchi, A. P. Wijerathna, M. Thakurdesai, J. Preston, I. Albinsson, B.E. Mellander, High efficiency dye-sensitized solar cell based on a novel gel polymer electrolyte containing RbI and tetrahexylammonium iodide (Hex4NI) salts and multi-layered photoelectrodes of TiO2 nanoparticles, Renew. Sustain. Energy Rev. 103 (2019) 282–290.
[23] T.M.W.J. Bandara, H.M.N. Wickramasinghe, K. Wijayaratne, L.A. DeSilva, A.A. I. Perera, Quasi-solid-state dye-sensitized solar cells utilizing TiO_2/graphite composite counter electrode and TiO 2/N719 sensitizer photoelectrode for low-cost power generation, J. Mater. Sci.: Mater. Electron. 32 (2021) 26758–26769.
[24] K. Rahmani, G.H. Majzoobi, A. Sadooghi, M. Kashfi, Mechanical and physical characterization of Mg-TiO_2 and Mg-ZrO_2 nanocomposites produced by hot-pressing, Mater. Chem. Phys. 246 (2020) 122844.
[25] G. Zhang, Y. Chen, Y. Chen, H. Guo, Activated biomass carbon made from bamboo as electrode material for supercapacitors, Mater. Res. Bull. 102 (2018) 391–398.
[26] S. Aderyani, P. Flouda, S.A. Shah, M.J. Green, J.L. Lutkenhaus, H. Ardebili, Simulation of cyclic voltammetry in structural supercapacitors with pseudocapacitance behavior, Electrochim. Acta 390 (2021) 138822.
[27] C.S. Yang, Y.S. Jang, H.K. Jeong, Bamboo-based activated carbon for supercapacitor applications, Curr. Appl. Phys. 14 (12) (2014) 1616–1620.
[28] T.M.W.J. Bandara, T.M.A.A.B. Thennakoon, G.G.D.M.G. Gamachchi, L.R.A. K. Bandara, B.M.K. Pemasiri, U. Dahanayake, An electrochemical route to exfoliate vein graphite into graphene with black tea, Mater. Chem. Phys. 289 (2022) 126450.
[29] S. Saini, P. Chand, A. Joshi, Biomass derived carbon for supercapacitor applications, J. Energy Storage 39 (2021) 102646.
[30] C. Peng, X.B. Yan, R.T. Wang, J.W. Lang, Y.J. Ou, Q.J. Xue, Promising activated carbons derived from waste tea-leaves and their application in high performance supercapacitors electrodes, Electrochim. Acta 87 (2013) 401–408.
[31] L.H. Wang, M. Toyoda, M. Inagaki, Dependence of electric double layer capacitance of activated carbons on the types of pores and their surface areas, New Carbon Materials 23 (2) (2008) 111–115.
[32] A.J. Bard, L.R. Faulkner, H.S. White, Electrochemical methods : Fundamentals and Applications, John Wiley & Sons, 2022.

[33] M.D. Stoller, R.S. Ruoff, Best practice methods for determining an electrode material's performance for ultracapacitors, Energy Environ. Sci. 3 (9) (2010) 1294–1301.
[34] L. Demarconnay, E. Raymundo-Piñero, F. Béguin, A symmetric carbon/carbon supercapacitor operating at 1.6 V by using a neutral aqueous solution, Electrochem. Commun. 12 (10) (2010) 1275–1278.
[35] C. Ramasamy, J.P.D. Val, M. Anderson, An analysis of ethylene glycol-aqueous based electrolyte system for supercapacitor applications, J. Power. Source. 248 (2014) 370–377.
[36] D. Jiménez-Cordero, F. Heras, M.A. Gilarranz, E. Raymundo-Piñero, Grape seed carbons for studying the influence of texture on supercapacitor behaviour in aqueous electrolytes, Carbon N. Y. 71 (2014) 127–138.
[37] Q. Abbas, D. Pajak, E. Frąckowiak, F. Béguin, Effect of binder on the performance of carbon/carbon symmetric capacitors in salt aqueous electrolyte, Electrochim. Acta 140 (2014) 132–138.
[38] Y. Mun, C. Jo, T. Hyeon, J. Lee, K.-S. Ha, K.-W. Jun, S.-H. Lee, et al., Simple synthesis of hierarchically structured partially graphitized carbon by emulsion/block-copolymer co-template method for high power supercapacitors, Carbon N. Y. 64 (2013) 391–402.
[39] Z. Jin, X. Yan, Y. Yu, G. Zhao, Sustainable activated carbon fibers from liquefied wood with controllable porosity for high-performance supercapacitors, J. Mater. Chem. A 2 (30) (2014) 11706–11715.
[40] H. Xu, L. Wang, Y. Zhang, Y. Chen, S. Gao, Pore-structure regulation of biomass-derived carbon materials for an enhanced supercapacitor performance, Nanoscale 13 (22) (2021) 10051–10060.
[41] A. Jain, M. Ghosh, M. Krajewski, S. Kurungot, M. Michalska, Biomass-derived activated carbon material from native European deciduous trees as an inexpensive and sustainable energy material for supercapacitor application, J. Energy Storage 34 (2021) 102178.
[42] H. Wang, H. Wang, F. Ruan, Q. Feng, Y. Wei, J. Fang, High-porosity carbon nanofibers prepared from polyacrylonitrile blended with amylose starch for application in supercapacitors, Mater. Chem. Phys. 293 (2023) 126896.
[43] Q. Liang, J. Wan, P. Ji, D. Zhang, N. Sheng, S. Chen, H. Wang, Continuous and integrated PEDOT@ Bacterial cellulose/CNT hybrid helical fiber with "reinforced cement-sand" structure for self-stretchable solid supercapacitor, Chem. Eng. J. 427 (2022) 131904.
[44] M.S. Wu, M.J. Wang, J.J. Jow, Fabrication of porous nickel oxide film with open macropores by electrophoresis and electrodeposition for electrochemical capacitors, J. Power Source. 195 (12) (2010) 3950–3955.
[45] X. Xiong, J. Chen, D. Zhang, A. Li, J. Zhang, X. Zeng, Hetero-structured nanocomposites of Ni/co/O/S for high-performance pseudo-supercapacitors, Electrochim. Acta 299 (2019) 298–311.
[46] I. Albinsson, B.E. Mellander, J.R. Stevens, Ion association effects and ionic conductivity in polymer electrolytes, Solid. State Ion. 60 (1-3) (1993) 63–66.
[47] S. Biniak, G. Szymański, J. Siedlewski, A. Świątkowski, The characterization of activated carbons with oxygen and nitrogen surface groups, Carbon N. Y. 35 (12) (1997) 1799–1810.
[48] H. Liu, A. Imanishi, Y. Nakato, Mechanisms for photooxidation reactions of water and organic compounds on carbon-doped titanium dioxide, as studied by photocurrent measurements, J. Phys. Chem. C 111 (24) (2007) 8603–8610.
[49] Z. He, W. Que, J. Chen, Y. He, G. Wang, Surface chemical analysis on the carbon-doped mesoporous TiO2 photocatalysts after post-thermal treatment: XPS and FTIR characterization, J. Phys. Chem. Solid. 74 (7) (2013) 924–928.
[50] D.-e. Gu, Y. Lu, B.-c. Yang, Facile preparation of micro–mesoporous carbon-doped TiO_2 photocatalysts with anatase crystalline walls under template-free condition, Chem. Commun. 21 (2008) 2453–2455.
[51] W. Mai, F. Wen, D. Xie, Y. Leng, Z. Mu, Structure and composition study of carbon-doped titanium oxide film combined with first principles, J. Adv. Ceram. 3 (2014) 49–55.
[52] V. Natu, M. Benchakar, C. Canaff, A. Habrioux, S. Celerier, M.W. Barsoum, A critical analysis of the X-ray photoelectron spectra of Ti3C2Tz MXenes, Matter. 4 (4) (2021) 1224–1251.
[53] J. Yang, J. Li, Synthesis, characterization and degradation of Bisphenol A using Pr, N Juan, Jun Dai, and co-doped TiO_2 with highly visible light activity, Appl. Surf. Sci. 257 (21) (2011) 8965–8973.